Comparative Nonlinear Observability Analysis of Spatial Discretization Schemes for Lithium-Ion Battery Models

Joseph N. E. Lucero[1], *Graduate Student Member, IEEE* and Simona Onori[2], *Senior Member, IEEE*

***Abstract*— Lithium-ion batteries are critical for modern energy storage systems, with accurate modeling essential for optimized performance, safety, and operational life. This paper investigates how the choice of spatial discretization method for the widely-used, partial differential equation-based, single-particle model affects the nonlinear observability properties of electrochemical model-based observers. Despite different spatial discretization schemes achieving similar voltage prediction accuracy with respect to experimental data, the choice of scheme leads to state-space representations that have different observability properties. We also find that increasing the number of states of the internal model decreases the expected quality of the state estimates, as the newly introduced states tend to be nearly redundant copies of existing states. These findings emphasize the importance of balancing model complexity, experimental accuracy, and nonlinear observability—an often-overlooked aspect—when selecting electrochemical models for observer design. Greater attention to nonlinear observability could lead to more effective and reliable battery management systems.**

I. INTRODUCTION

Lithium-ion batteries (LIBs) are integral to modern energy storage systems, powering technologies ranging from portable electronics to electric vehicles and grid-scale applications [1]. As demand for high-performance, reliable battery systems continues to grow, accurate modeling of lithium-ion battery behavior is recognized as the root of the ability to ensure optimized performance, safety, and operational life. Electrochemical-based observers, which leverage physics-based models to estimate the internal electrochemical states of LIBs, are a promising alternative to traditional empirical model-based observers [2], [3]. They hold potential to play a more prominent role in battery management systems (BMS) due to their ability to provide a deeper understanding of battery behavior and offer the potential for more accurate predictions of key battery states, such as state of charge (SoC) and state of health (SoH), which are critical for efficient control and safe operation [4].

The effectiveness of any observer is tightly linked to the choice of state-space representation for the physical system of interest. In particular, the (nonlinear) observability properties of the chosen state-space representation dictate the estimation performance of observers built on this representation. In the context of LIB observers, the choice of: 1) electrochemical model consistent with the inputs and outputs, as well as 2) how the governing equations are spatially discretized, constitutes the representation of the system. The analysis in this work assumes that the set of inputs and measurements (via output sensors) are fixed: The input is an applied current and the output is a measurement of the terminal voltage. A reduced-order model of lithium-ion dynamics within the battery cell known as the single-particle model (SPM) [5] provides a balance between complexity and accuracy and is the focus of our analysis here. The literature has paid considerably less attention to how the choice of spatial discretization scheme—used to convert the governing partial differential equations (PDE) of the SPM model into ordinary differential equations (ODE) for numerical simulation—impacts the observability of the resulting state-space representation.

While some studies have explored the nonlinear observability of battery models, they have primarily focused on how the number of discretization points affects observability for a fixed discretization scheme [6], without systematically investigating the influence of the discretization scheme itself. We address this gap by extending previous work of [2], [6] to explore how the choice of particular discretization method for the SPM affects the final model's nonlinear observability properties. Interestingly, though counterintuitively, we find that spatial discretization methods previously been shown to have greater accuracy in recapitulating experimentally observed voltage dynamics in simulation [7] result in a state-space representation where the system's internal states are more difficult to estimate. We show that observer designs which estimate the lithium concentration in each electrode separately (such as the interconnected electrode observer proposed in [3]) are expected to provide higher quality estimates of the internal electrochemical states relative to observer designs that attempt the inference of lithium concentration in both electrodes.

Ultimately, this work highlights how the spatial discretization of an electrochemical model impacts an observer's ability to estimate the battery's internal states. A thorough understanding of how observability properties change under different modeling choices is crucial for successful deployment of these models in BMS applications.

II. NONLINEAR OBSERVABILITY

Nonlinear observability for battery models has previously been explored and characterized for ECMs [8] and electrochemical models [2], [6]. In this section, we summarize the salient concepts of nonlinear observability relevant to

[1]Joseph N. E. Lucero is with the Department of Chemistry, Stanford University, Stanford, CA 94305, USA. jlucero@stanford.edu

[2]Simona Onori is with the Department of Energy Science & Engineering, Stanford University, Stanford CA 94305, USA. sonori@stanford.edu

the present discussion while establishing our notations and conventions.

The PDE-based governing equation of SPM electrochemical model, using method of lines [9] and a spatial discretization scheme, can be brought to a state-space representation of the following form[1]:

$$\begin{aligned} \dot{\mathbf{x}} &= A\mathbf{x} + Bu \\ y &= h(\mathbf{x}, u) \ , \end{aligned} \tag{1}$$

where the state vector $\mathbf{x} \in \mathbb{R}^n$ contains a number of states n, the scalar input is $u \in \mathbb{R}$, and $h : \mathbb{R}^n \times \mathbb{R} \to \mathbb{R}$ is the scalar nonlinear output, which is a function of both the states and the input. We focus on the class of electrochemical battery models that can be reduced to a state-space model that is linear in the states but remains nonlinear in its output [10]. Further, for this model, the system matrix $A \in \mathbb{R}^{n\times n}$ can be decomposed as a product of three matrices $\mathcal{M}^{-1}, \mathcal{A}, \ \mathcal{D} \in \mathbb{R}^{n\times n}$: $A = \mathcal{M}^{-1}\mathcal{A}\mathcal{D}$. Hereafter, we refer to the matrix $\mathcal{M}$ as the "mass matrix", $\mathcal{A}$ as the "area-weighting matrix", and $\mathcal{D}$ as the "differentiation matrix". Similarly, the input vector is computed as a matrix-vector product, $B = \mathcal{M}^{-1}\mathcal{B}$, where $\mathcal{B} \in \mathbb{R}^n$ is a vector. The specific forms of these matrices are determined by the choice of spatial discretization scheme as described in Section III below.

Observability is a structural property of the chosen system representation, that guarantees that the initial internal states of a dynamical system can be inferred based on the input and output sensor measurements [11]. If a system is observable then an observer can, in principle, be designed to infer the internal states of the dynamical system. A given representation of a nonlinear system, such as in (1), is defined to have "weak local observability" if

$$\text{rank}\left(\mathcal{O}|_{\mathbf{x}^*}\right) = n \qquad \text{"Observability rank test"} \tag{2}$$

where $\mathcal{O} \in \mathbb{R}^{n\times n}$ is the "nonlinear observability matrix" computed as the state Jacobian of the $n-1$ Lie derivatives evaluated at specific points in state space $\mathbf{x}^*$,

$$\mathcal{O}|_{\mathbf{x}^*} = \frac{\partial}{\partial \mathbf{x}} \left(\begin{bmatrix} y & \dot{y} & \ddot{y} & \cdots & y^{(n-1)} \end{bmatrix}^{\mathrm{T}} \right) \Big|_{\mathbf{x}^*} , \tag{3}$$

for each time $t \in [0, T_{\text{end}}]$ [12]. In this work, the computer algebra software `Mathematica (version 14.1)` [13] is used to evaluate (3) and obtain explicit formulas for the elements of the observability matrix.

While the rank test of the observability matrix may determine if the the chosen system representation definitively attains weak local observability, the condition number[2],

$$\kappa(\mathcal{O}|_{\mathbf{x}^*}) = ||(\mathcal{O}|_{\mathbf{x}^*})^{-1}|| \cdot ||\mathcal{O}|_{\mathbf{x}^*}|| \ , \tag{4}$$

is used as a quantification of the quality of the state estimates that can be inferred from the input and output sensor data. Intuitively, if a particular state is weakly observable this implies small changes in this state will lead to insignificant changes in the output and its time derivatives. In evaluating the Jacobian of the vector of output time derivatives in (3) to obtain the observability matrix, if a weakly observable state is present then one column of the observability matrix will be significantly smaller in magnitude than the others, leading to an ill-conditioned matrix and thus a high condition number [14]. As a result, if some noise is present in the measurement y—leading to a finite signal-to-noise ratio [15]—minor variations in the measurement due to the noise can significantly impact the initial state estimate [16].

[1]Throughout this paper, italicized variables indicate scalars, boldfaced variables indicate vectors, capitalized variables indicate matrices, and overdots on variables is shorthand for time derivatives (e.g., $\dot{\mathbf{x}} = \mathrm{d}\mathbf{x} \,/\, \mathrm{d}t$).

[2]We consider the induced 2-norm in computing matrix condition numbers in this work: $||\cdot|| = ||\cdot||_2$.

III. SINGLE-PARTICLE MODEL

The SPM reduces model complexity by assuming that each of the battery electrodes is comprised of spherical particles that have the same radius. By virtue of this assumption, the behavior of lithium within all of the particles of a particular electrode can be determined by tracking the lithium dynamics within just one of the particles [17]. Thus, the negative and positive electrodes $i = \{\mathrm{n}, \mathrm{p}\}$ in this model are each represented by a single spherical particle with radius $R_{\mathrm{s},i}$.

The lithium concentration within a given electrode particle is assumed to evolve according to Fick's law of diffusion (5), under a constant diffusion constant $D_{\mathrm{s},i}$ [10]. At the surface of the electrode particle, the intercalation/deintercalation of lithium from/to the surrounding (implicit) electrolyte is assumed to be governed by the Butler-Volmer equation, assuming a charge-transfer coefficient of $\alpha = 1/2$ and characterized by the electrode overpotential η_i, which itself is dependent on the surface lithium concentration of the electrode particle $c_{\mathrm{s},i}^{\mathrm{surf}} = c_{\mathrm{s},i}(r = R_{\mathrm{s},i}, t)$, the input current I_{app} and the thermal voltage $V_{\mathrm{th}} = 25.69$ mV, assuming a constant battery operating temperature of 25 °C. In this model, any lithium concentration dynamics other than those that occur in the solid-phase electrode particles are considered negligible: The lithium concentration in the electrolyte is assumed to be fixed to an average value of $c_e^{\mathrm{avg}} = 1000$ [7]. The set of governing equations of the SPM is summarized in Table I.

A. Radial discretization

To solve the lithium dynamics described by the SPM, the mass-transport equation (5) must be discretized. To this end, the radius of each spherically-symmetric electrode particle is discretized into N_r number of nodes, where the distance of the jth node from the center of the particle is,

$$r_j^i = (j-1)\Delta r_i, \ \ j \in [1, 2, \ldots, N_r] \ . \tag{12}$$

The first node ($j = 1$) is located at the center of the particle, while the final node ($j = N_r$) is located at the particle surface. The finite radius R_i of each representative particle for electrode $i \in \{\mathrm{n}, \mathrm{p}\}$ determines the spacing between the nodes,

$$\Delta r_i = R_i / \left(N_r - 1\right) \ . \tag{13}$$

We specialize to the case where the number of nodes is used to discretize both electrodes; however, the radii of each representative particle is in general different, i.e., $R_{\mathrm{s,p}} \neq$

TABLE I

GOVERNING EQUATIONS OF THE SPM

Variable	Equation	
Fick's Law of Diffusion	$N_i(r,t) = -D_{\mathrm{s},i}\frac{\partial c_{\mathrm{s},i}}{\partial r}, \quad i = \{\mathrm{n},\mathrm{p}\}$	(5)
Mass transport in solid phase	$\frac{\partial c_{\mathrm{s},i}}{\partial t} = -\boldsymbol{\nabla}\cdot N_i$	(6)
Boundary conditions	$N_i(r=0,t)=0; \quad N_i(r=R_{\mathrm{s},i},t) = \frac{I_{\mathrm{app}} g_i}{a_{\mathrm{s},i} A_{\mathrm{cell}} L_i F}$ $a_{\mathrm{s},i} = \frac{3}{R_{\mathrm{s},i}}\varepsilon_i, \qquad g_i = \begin{cases} -1, & i=\mathrm{p} \\ 1, & i=\mathrm{n} \end{cases}$	(7)
Electrode overpotential	$\eta_i = 2\cdot V_{\mathrm{th}}\cdot \sinh^{-1}\left(\frac{I_{\mathrm{app}} g_i}{2 a_{s,i} A L_i F j_{0,i}}\right),$	(8)
Exchange flux density	$j_{0,i} = k_{0,i}\sqrt{c_{\mathrm{e}}^{\mathrm{avg}}\left(\frac{c_{\mathrm{s},i}^{\mathrm{surf}}}{c_{\mathrm{s},i}^{\mathrm{max}}}\right)\left(1-\frac{c_{\mathrm{s},i}^{\mathrm{surf}}}{c_{\mathrm{s},i}^{\mathrm{max}}}\right)}$	(9)
Cell voltage	$V_{\mathrm{cell}} = U_{\mathrm{p}}\left(\frac{c_{\mathrm{s,p}}^{\mathrm{surf}}}{c_{\mathrm{s,p}}^{\mathrm{max}}}\right) - U_{\mathrm{n}}\left(\frac{c_{\mathrm{s,n}}^{\mathrm{surf}}}{c_{\mathrm{s,n}}^{\mathrm{max}}}\right) + \eta_{\mathrm{p}} - \eta_{\mathrm{n}} - R_\ell \cdot I_{\mathrm{app}}$	(10)
State-of-Charge	$\theta_{\mathrm{s,p}}^{\mathrm{bulk}} = \frac{1}{\frac{4}{3}\pi R_{\mathrm{s,p}}^3}\int_{V_{\mathrm{n}}^{\mathrm{sphere}}}\left(\frac{c_{\mathrm{s,p}}}{c_{\mathrm{s,p}}^{\mathrm{max}}}\right)\mathrm{d}V$ $\theta_{\mathrm{s,n}}^{\mathrm{bulk}} = \frac{1}{\frac{4}{3}\pi R_{\mathrm{s,n}}^3}\int_{V_{\mathrm{p}}^{\mathrm{sphere}}}\left(\frac{c_{\mathrm{s,n}}}{c_{\mathrm{s,n}}^{\mathrm{max}}}\right)\mathrm{d}V$ $\mathrm{SoC_p} = \frac{\theta_{\mathrm{s,p}}^{0\%} - \theta_{\mathrm{s,p}}^{\mathrm{bulk}}}{\theta_{\mathrm{s,p}}^{0\%} - \theta_{\mathrm{s,p}}^{100\%}}, \quad \mathrm{SoC_n} = \frac{\theta_{\mathrm{s,n}}^{\mathrm{bulk}} - \theta_{\mathrm{s,n}}^{0\%}}{\theta_{\mathrm{s,n}}^{100\%} - \theta_{\mathrm{s,n}}^{0\%}}$	(11)

$R_{\mathrm{s,n}}$. Our analysis will also require consideration of points in between the N_r discrete nodes. For notational convenience, we annotate these halfway points between nodes as,

$$r_{j+1/2}^i \equiv (r_j + r_{j+1})/2, \ 1 \le j \le N_r - 1 \tag{14a}$$
$$= r_j^i + (\Delta r_i/2) \ . \tag{14b}$$

B. Output equation

The output of an electrochemical-based LIB model is the terminal cell voltage of the LIB,

$$y_{\mathrm{cell}} = y_{\mathrm{p}} - y_{\mathrm{n}} - R_\ell u \ , \tag{15}$$

which accounts for each electrode's voltage,

$$y_i = U_i\left(c_{\mathrm{s},i}^{\mathrm{surf}}/c_{\mathrm{s},i}^{\mathrm{max}}\right) + \eta_i\left(c_{\mathrm{s},i}^{\mathrm{surf}}/c_{\mathrm{s},i}^{\mathrm{max}}, u\right) \ , \tag{16}$$

and a lumped contact resistance R_ℓ. The open-circuit potential (OCP) of the electrode i is denoted as U_i. In this work, we focus on the LG INR21700-M50T NMC/Gr 21700 cell with a capacity of 4.85 Ah with its positive and negative OCPs characterized and reported in [18].

C. Numerical Methods

Having discretized the radial coordinate into a one-dimensional grid according to (12), there remains a choice of how to spatially discretize the mass-transport equation (5) onto this grid. In the following, we discuss three commonly used methods to perform this discretization.

1) Finite Difference Method: The finite difference method (FDM) directly discretizes the derivatives in the mass-transport equation using finite differences. This results in a system of the form (1) where the state vector for each electrode i consists of the concentration $c_{\mathrm{s},i,j} = c_{\mathrm{s},i}(r = r_j, t)$ at the discrete nodes, $\mathbf{x}_i^{\mathrm{FDM}} = \begin{bmatrix} c_{\mathrm{s},i,1} & c_{\mathrm{s},i,2} & \cdots & c_{\mathrm{s},i,N_r} \end{bmatrix}^{\mathrm{T}}$. The surface concentrations for this method can be obtained from the concentration of the node point on the surface: $c_{\mathrm{s},i}^{\mathrm{surf,FDM}} = c_{\mathrm{s},i,N_r}$. The mass and area-weighting matrices for both electrodes $\mathcal{M}_{\mathrm{n}}^{\mathrm{FDM}} = \mathcal{M}_{\mathrm{p}}^{\mathrm{FDM}} = \mathcal{A}_{\mathrm{n}}^{\mathrm{FDM}} = \mathcal{A}_{\mathrm{p}}^{\mathrm{FDM}} = \mathbb{I}$ are all equal to the identity matrix in this scheme. The differentiation matrix $\mathcal{D}_i^{\mathrm{FDM}}$ for this method is a tridiagonal matrix where jth row and the kth column have elements defined according to,

$$\frac{(\mathcal{D}_i^{\mathrm{FDM}})_{jk}}{D_{\mathrm{s},i}/(\Delta r_i)^2} = \begin{cases} -6, & j=1, \ k=j \\ 6, & j=1, \ k=j+1 \\ \left(1-\frac{1}{2(j-1)}\right)^2, & 1<j<N_r, \ k=j-1 \\ -\left(2+\frac{1}{2(j-1)^2}\right), & 1<j\le N_r, \ k=j \\ \left(1+\frac{1}{2(j-1)}\right)^2, & 1<j<N_r, \ k=j+1 \\ \left(2+\frac{1}{2(N_r-1)^2}\right), & j=N_r, \ k=j-1 \\ 0, & \text{otherwise} \ . \end{cases} \tag{17}$$

The vector $\mathcal{B}_i^{\mathrm{FDM}}$ for each electrode is defined as,

$$(\mathcal{B}_i^{\mathrm{FDM}})_j = \begin{cases} \frac{2}{\Delta r_i}\left(1+\frac{1}{2(N_r-1)}\right)^2 \frac{g_i}{a_{\mathrm{s}}^{(i)} L_i A F}, & j = N_{\mathrm{r}} \\ 0, & \text{otherwise} \ , \end{cases} \tag{18}$$

with

$$g_i = \begin{cases} 1, & i = \mathrm{n} \\ -1, & i = \mathrm{p} \ . \end{cases} \tag{19}$$

2) Finite Volume Method: The finite volume method (FVM) is an alternative spatial discretization method that proceeds by first volume-averaging the mass-transport equation and applying the divergence theorem yielding,

$$V_{j+1/2} \times \dot{\bar{c}}_{\mathrm{s},j+1/2} = -\left[\int_{A_{j+1}} N \,\mathrm{d}A - \int_{A_{j+1}} N \,\mathrm{d}A\right] \ . \tag{20}$$

Discretizing this equation results in a system of the form (1) where the state vector $\mathbf{x}_i^{\mathrm{FVM}} = \begin{bmatrix} \bar{c}_{\mathrm{s},i,1+1/2} & \bar{c}_{\mathrm{s},i,2+1/2} & \cdots & \bar{c}_{\mathrm{s},i,N_{\mathrm{FV}}+1/2} \end{bmatrix}^{\mathrm{T}}$ contains the average concentration $\bar{c}_{\mathrm{s},i,j+1/2} = \bar{c}_{\mathrm{s},i}(r = r_{j+1/2}, t)$ of each "finite volume", defined to be the spherical shell with $r \in [r_j^i, r_{j+1}^i]$ centered on the point $r_{j+1/2}^i$ and having a volume of,

$$V_{j+1/2} = \tfrac{4\pi}{3}\left((r_{j+1}^i)^3 - (r_j^i)^3\right), \ 1 \le j \le N_{\mathrm{FV}} \ . \tag{21}$$

As the edges of each finite volume are the number of nodes defined in (12), there are a total of $N_{\mathrm{FV}} = N_r - 1$ finite volumes given a number of nodes N_r. A feature of the FVM is that, unlike the FDM and the control volume method discussed in the next section, an estimate of the surface concentration $c_{\mathrm{s},i}^{\mathrm{surf}}$ is not directly available. Thus, the method must also be furnished by an extrapolation scheme that uses information from the states nearest to the surface of the particle to estimate the surface concentration. In this work, we consider the Hermite-polynomial-based method first described in [7] and given as,

$$c_{\mathrm{s},i}^{\mathrm{surf,FVM}} = \frac{15}{8}\bar{c}_{\mathrm{s},i,N_{\mathrm{FV}}+1/2} - \frac{10}{8}\bar{c}_{\mathrm{s},i,(N_{\mathrm{FV}}-1)+1/2} + \frac{3}{8}\bar{c}_{\mathrm{s},i,(N_{\mathrm{FV}}-2)+1/2} \tag{22}$$

Following the discretization procedure described above leads to a diagonal mass matrix for this method,

$$(\mathcal{M}_i^{\mathrm{FVM}})_{jk} = \begin{cases} V_{j+1/2}, & 1 \le j \le N_{\mathrm{FV}}, \ k=j \\ 0, & \text{otherwise} \ . \end{cases} \tag{23}$$

Notably, each column of the mass matrix trivially sums to the volume of the corresponding shell indicating that lithium mass is conserved with the correct volume. The area-weighting matrix is defined as,

$$(\mathcal{A}_i^{\mathrm{FVM}})_{jk} = \begin{cases} -A_{j+1}, & 1 \leq j \leq N_{\mathrm{FV}} - 1,\ k = j \\ A_j, & 1 < j \leq N_{\mathrm{FV}} - 1,\ k = j - 1 \\ 0, & \text{otherwise}\ . \end{cases} \tag{24}$$

where, notably, its right-most column is entirely zeros and each column of the matrix sums to zero. The differentiation matrix is defined according to

$$\frac{(\mathcal{D}_i^{\mathrm{FVM}})_{jk}}{D_{\mathrm{s},i}/\Delta r_i} = \begin{cases} 1, & 1 \leq j \leq N_{\mathrm{FV}} - 1,\ k = j \\ -1, & 1 < j \leq N_{\mathrm{FV}} - 1,\ k = j + 1 \\ 0, & \text{otherwise}\ , \end{cases} \tag{25}$$

whose bottom-most row is filled with zeros and each row of the matrix sums to zero. The vector $\mathcal{B}_i$ for this method is,

$$(\mathcal{B}_i^{\mathrm{FVM}})_{jk} = \begin{cases} A_{N_{\mathrm{FV}}} \frac{g_i}{a_{s,i} L_i A F}, & j = N_{\mathrm{FV}} \\ 0, & \text{otherwise}\ . \end{cases} \tag{26}$$

3) Control Volume Method: The control volume method (CVM) is obtained in a similar manner to the FVM where the volume-averaged form of the mass-transport equation is considered [19]; however, the derivation differs in that the volumes it considers are spherical shells $r \in [r_{j-1/2}, r_{j+1/2}]$ centered on the node point r_j with a volume of,

$$V_j = \frac{4\pi}{3} \begin{cases} \left(r^i_{1+1/2}\right)^3, & j = 1 \\ \left(r^i_{N_r}\right)^3 - \left(r^i_{(N_r-1)+1/2}\right)^3, & j = N_r \\ \left(r^i_{j+1/2}\right)^3 - \left(r^i_{j-1/2}\right)^3, & 1 < j < N_r\ . \end{cases} \tag{27}$$

Importantly, the volumes of the states at the edges of the grid are treated differently to the interior nodes. Additionally, to guarantee lithium mass conservation, the mass matrix definition is modified to preserve the necessary column sum property:

$$(\mathcal{M}_i^{\mathrm{CVM}})_{jk} = \begin{cases} V_1/4, & j = 2,\ k = j - 1 \\ V_{N_r}/4, & j = N_r - 1,\ k = j + 1 \\ V_j/8, & 2 < j < N_r,\ k = j - 1 \\ V_j/8, & 1 < j < N_r - 1,\ k = j + 1 \\ 3V_j/4, & 1 \leq j \leq N_r,\ k = j \\ 0, & \text{otherwise}\ . \end{cases} \tag{28}$$

Unlike the FVM, the mass matrix of the CVM is tridiagonal in structure. The area-weighting matrix has a similar structure to that in the FVM,

$$(\mathcal{A}_i^{\mathrm{CVM}})_{jk} = \begin{cases} -A_{j+1/2}, & 1 \leq j \leq N_r - 1,\ k = j \\ A_{j+1/2}, & 1 < j \leq N_r - 1,\ k = j - 1 \\ 0, & \text{otherwise}\ . \end{cases} \tag{29}$$

Similarly, the differentiation matrix,

$$\frac{(\mathcal{D}_i^{\mathrm{CVM}})_{jk}}{D_{\mathrm{s},i}/\Delta r_i} = \begin{cases} 1, & 1 \leq j \leq N_r - 1,\ k = j \\ -1, & 1 < j \leq N_r - 1,\ k = j + 1 \\ 0, & \text{otherwise}\ , \end{cases} \tag{30}$$

and $\mathcal{B}_i$ vector, retains similar forms to their FVM counterparts.

$$(\mathcal{B}_i^{\mathrm{CVM}})_{jk} = \begin{cases} A_{N_r} \frac{g_i}{a_{s,i} L_i A F}, & j = N_r \\ 0, & \text{otherwise}\ . \end{cases} \tag{31}$$

This construction endows CVM method with a similar state vector as that of the FDM method but with average volume concentration as the states, $\mathbf{x}_i^{\mathrm{CVM}} = \begin{bmatrix} \bar{c}_{\mathrm{s},i,1} & \bar{c}_{\mathrm{s},i,2} & \cdots & \bar{c}_{\mathrm{s},i,N_r} \end{bmatrix}^{\mathrm{T}}$. The surface concentration in this method can be obtained from the last state in the state vector: $c_{\mathrm{s},i}^{\mathrm{surf,CVM}} = \bar{c}_{\mathrm{s},i,N_r}$

D. Electrode vs. full-cell observers

For the purpose of the observability analysis performed later in Section IV, we introduce here a distinction between an "electrode-level observer" and a "full-cell observer". Explicitly, an electrode-level observer monitors only the state dynamics of one of the electrodes. Thus, for this type of observer, the state dynamics are governed by (1) with the relevant matrices and vectors $\mathcal{M}_i$, $\mathcal{A}_i$, $\mathcal{D}_i$, and $\mathcal{B}_i$ being electrode dependent. Furthermore, the output of a given electrode observer is only the electrode voltage (16)

The full-cell observer, on the other hand, considers the state vector containing the concentrations at both electrodes[3], $\mathbf{x}^m = \begin{bmatrix} \mathbf{x}_{\mathrm{n}}^m & \mathbf{x}_{\mathrm{p}}^m \end{bmatrix}^{\mathrm{T}}$. Here, the superscript $m \in \{\mathrm{FDM}, \mathrm{FVM}, \mathrm{CVM}\}$ indexes the different spatial discretization methods. The system matrix A for the the full-cell observer evolves the lithium concentration at both electrodes simultaneously and is obtained from $\mathcal{M}_i^m$, $\mathcal{A}_i^m$ and $\mathcal{D}_i^m$ matrices, which are arranged in a block-diagonal fashion,

$$\mathcal{M}^m = \begin{bmatrix} \mathcal{M}_{\mathrm{n}}^m & \mathbf{0} \\ \mathbf{0} & \mathcal{M}_{\mathrm{p}}^m \end{bmatrix}, \tag{32a}$$

$$\mathcal{A}^m = \begin{bmatrix} \mathcal{A}_{\mathrm{n}}^m & \mathbf{0} \\ \mathbf{0} & \mathcal{A}_{\mathrm{p}}^m \end{bmatrix}, \tag{32b}$$

$$\mathcal{D}^m = \begin{bmatrix} \mathcal{D}_{\mathrm{n}}^m & \mathbf{0} \\ \mathbf{0} & \mathcal{D}_{\mathrm{p}}^m \end{bmatrix}. \tag{32c}$$

The $\mathcal{B}^m$ vector is a concatenation of the individual electrode $\mathcal{B}_i^m$ vectors, $\mathcal{B}^m = \begin{bmatrix} \mathcal{B}_{\mathrm{n}}^m & \mathcal{B}_{\mathrm{p}}^m \end{bmatrix}^{\mathrm{T}}$. The full-cell observers consider (15) as the output equation for its internal LIB model.

E. Calibration procedure

Given a chosen combination of number of states for each electrode and spatial discretization scheme, we calibrate the resulting state-space models to experimental data which was collected and reported in [20]. We direct the reader to our previous publications [7], [21] for further details on how model calibration is performed. Briefly, we use particle-swarm optimization to vary a subset of the model's physical parameters in order to minimize the root-mean-square percent voltage error (RMSPE) between the model's predicted cell-level voltage and the experimentally-measured voltage,

$$\frac{\mathrm{RMSPE}}{10^2} = \sqrt{\frac{1}{N_{\mathrm{meas}}} \sum_{s=1}^{N_{\mathrm{meas}}} \left[1.0 - \left(y_{\mathrm{cell}}(s\Delta t)/V_{\mathrm{cell}}^{\mathrm{data}}(s\Delta t)\right)\right]^2}, \tag{33}$$

as well as the deviation of the predicted state-of-charge (SoC) for each electrode to the experimentally obtained SoC. Here, N_{meas} measurements comprising the data signal. For calibration, we use data from a hybrid power-pulse characterization (HPPC) test. To validate the calibrated models, we run them in an open-loop fashion under an urban dynamometer driving schedule (UDDS) input profile and compare the predicted voltage with experimental data.

IV. RESULTS

In this section, the results of the model calibration and validation are presented. Subsequently, how the choice of spatial discretization scheme, as well as the choice of the number of states, changes the associated observability properties is explored.

[3]Note: cell-level vectors and matrices do not have subscripts

A. Calibration metrics

Table II summarizes the RMSPE values obtained after calibration and validation for each combination of number of states and choice of discretization scheme. Uniformly, for both calibration and validation, we observe that all the models can achieve a RMSPE below 1% indicating a generally good fit to experimental data.

TABLE II

HPPC CALIBRATION AND UDDS VALIDATION ROOT-MEAN-SQUARE PERCENT VOLTAGE ERROR (33) BETWEEN MODEL PREDICTION AND EXPERIMENTAL DATA.

	n value	FDM	FVM	CVM
HPPC Calibration	6	0.78 %	0.66 %	0.52 %
	8	0.78 %	0.80 %	0.59 %
	10	0.80 %	0.55 %	0.60 %
UDDS Validation	6	0.69 %	0.53 %	0.75 %
	8	0.68 %	0.88 %	0.60 %
	10	0.85 %	0.47 %	0.53 %

B. Observability rank test

Having calibrated the models independently, with each model having different parameters that match its output to experimentally collected data, we consider the observability properties of each model. To this end, each of the models are subjected to a C/2 discharge from a 100% SoC for 6,480 seconds and we compute the observability matrix for the system states recorded along this trajectory. For each of the spatial discretization methods, we compare the results of the observability rank test for both a positive and negative electrode observer, as well as for a full-cell observer.

We find that across all choices of number of states and discretization schemes, for both electrode-level and full-cell observers, the observability matrix remains invertible for a variety of spatial discretization schemes. Importantly, the rank of a given matrix is (numerically) estimated by the number of singular values of the matrix that are greater than some tolerance. As such, the estimated rank of the observability matrix is quite sensitive to this choice of tolerance and careful consideration of what tolerance is acceptable for a given application is warranted. As our analysis here is application agnostic, we used a uniform tolerance of machine epsilon associated with double precision, $\varepsilon = 2.2204 \times 10^{-16}$.

C. Condition Number

Tolerance sensitivity in observability matrix rank estimation introduces ambiguity, necessitating an alternative metric for observer assessment. For this, we turn to the condition number of the observability matrix. In general, we find that, across the FDM (Fig. 1), FVM (Fig. 2), and CVM (Fig. 3) schemes, the observability matrices of the electrode-level observers attain much lower condition numbers than the observability matrix of the full-cell observer. This lends support to the initial findings of [6] that, for electrochemical-based observers of LIBs, an electrode-level observer design is expected to attain better performance compared to a full-cell observer design. Furthermore, we find in some cases, particularly for high number of internal states, that the observability matrix for an observer of one electrode has higher condition numbers than that of an observer for the opposite electrode (e.g., Fig. 3 for $N_r = 5$). This suggests that the difficulty of estimating the states may increase faster for one electrode relative to the other as the number of states increases. As such, having a non-equal number of states for each electrode may be beneficial.

In addition, we notice in general that the condition number tends to increase as the number of states in each electrode is increased for both the electrode-level and full-cell level observers. This is a result of states becoming "physically" closer together as the number

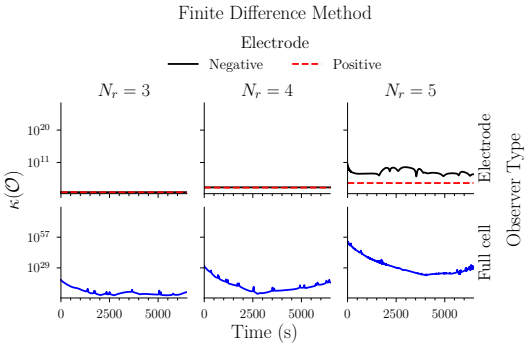

Fig. 1. Condition number of the observability matrix for an observer using FDM discretization. (Top row) Electrode-level observer. Black solid curve: condition numbers of the negative electrode observer. Red dashed curve: condition numbers of the positive electrode observer. (Bottom row) Full-cell observer. Number of states is increased in going left-to-right across columns of plots.

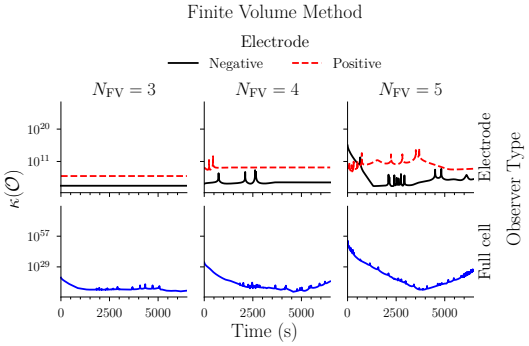

Fig. 2. Condition number of the observability matrix for an observer using FVM discretization. Same color scheme and variation as Fig. 1.

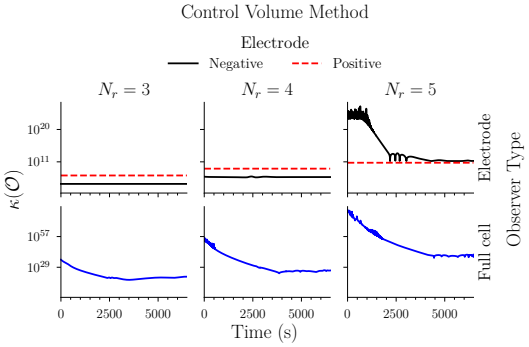

Fig. 3. Condition number of the observability matrix for an observer using CVM discretization. Same color scheme and variation as Fig. 1.

of states per electrode N_r is increased (cf. (13)). Consequently, adjacent states become similar in magnitude and begin to also dynamically evolve in a similar way since they are connected by a physical law (6). To quantify this, considering the FDM scheme, we measure the magnitude of the normalized discrepancy between the "nearest-to-center states", $|\Delta\theta_{\mathrm{s},i,\mathrm{center}}| = |c_{\mathrm{s},i,2} - c_{\mathrm{s},i,1}|/c_{\mathrm{s},i}^{\max}$. We find that this discrepancy is in the range of $|\Delta\theta_{\mathrm{s},i,\mathrm{center}}| \in (10^{-7}, 10^{-3})$ and is constant for the full discharge. In effect, since the output is only directly dependent on the surface concentration, by increasing the number of grid points in each electrode we add *nearly* redundant states and introduce more columns to the observability matrix that have much smaller magnitudes than the

columns associated with the states near the surface[4]. This addition leads to a greater disparity in singular values and is reflected by the increased condition number of the observability matrix for both electrode-level and full-cell observer.

Our results also show that the FDM discretization scheme generally yields observability matrices that achieve the lowest condition numbers across the discharge trajectory compared to the other two methods. In contrast, the observability matrix of the CVM scheme achieves the highest condition numbers indicating that estimating the CVM states is more difficult relative to estimating the states of the FDM scheme. This finding can be understood by examining the structure of the system matrix associated with each method. In the case of FDM and FVM the system matrices are tridiagonal, implying that exchange of concentration only occurs via directly adjacent nodes. Thus, for these schemes, while adjacent nodes may be difficult to distinguish from one another, adjacent nodes can be grouped together and these groupings can be distinguished from one another. In contrast, the system matrix of the CVM method is full. As such, the concentration dynamics of a single volume are coupled to the concentration for all other volumes. This makes it significantly more difficult to establish similar groupings of nodes for this scheme, thereby leading to a more difficult state estimation task and thus a higher condition number.

V. DISCUSSION

For LIBs, the choice of discretization and model parameters shapes the final system representation, directly influencing observer performance through its observability properties. We show that while different spatial discretization schemes and state counts can yield similar terminal voltage accuracy, they retain distinct observability characteristics, affecting the observer's ability to estimate states accurately despite matching experimental behavior.

This paper focuses on observability analysis for the SPM formulation in Table I, though alternative parameterizations exist that reduce the number of identifiable parameters [22]. The observability matrix condition number is highly sensitive to model parameters, as they directly affect the system matrix and input vector. Preliminary investigations suggest that while alternative parameterizations alter the condition number's absolute value, the trend of increasing condition number with more states remains unchanged. We are actively exploring these parameterizations in electrochemical models [23].

Our analysis here is limited to electrochemical models reducible to form (1), excluding other variants of electrochemical models [24], [25] that yield differential-algebraic equations after spatial discretization, requiring a separate observability analysis. We assume a fixed OCP representation [18]; however, different choices may alter observability characteristics, as seen in equivalent circuit-based observers [8]. Additionally, while we focus on spatial discretization's impact on observability properties, *temporal* discretization may also influence these properties along charge/discharge trajectories.

ACKNOWLEDGMENT

The authors thank Dr. Le Xu (Stanford Energy Science & Engineering) for helpful discussions.

REFERENCES

[1] S. J. Davis *et al.*, "Net-zero emissions energy systems," *Science*, vol. 360, no. 6396, p. eaas9793, Jun. 2018.

[2] A. Bartlett *et al.*, "Electrochemical Model-Based State of Charge and Capacity Estimation for a Composite Electrode Lithium-Ion Battery," *IEEE Trans. Contr. Syst. Technol.*, pp. 1–1, 2015.

[4]In contrast, ECMs inherently encode distinct time constants with added states, ensuring each contributes unique information. This prevents the observability matrix from becoming ill-conditioned, unlike PDE-based electrochemical models that require spatial discretization.

[3] A. Allam and S. Onori, "An Interconnected Observer for Concurrent Estimation of Bulk and Surface Concentration in the Cathode and Anode of a Lithium-ion Battery," *IEEE Trans. Ind. Electron.*, vol. 65, no. 9, pp. 7311–7321, Sep. 2018.

[4] N. A. Chaturvedi *et al.*, "Algorithms for Advanced Battery-Management Systems," *IEEE Control Syst.*, vol. 30, no. 3, pp. 49–68, Jun. 2010.

[5] S. Santhanagopalan and R. E. White, "Online estimation of the state of charge of a lithium ion cell," *Journal of Power Sources*, vol. 161, no. 2, pp. 1346–1355, Oct. 2006.

[6] A. Allam and S. Onori, "Linearized Versus Nonlinear Observability Analysis for Lithium-Ion Battery Dynamics: Why Respecting the Nonlinearities Is Key for Proper Observer Design," *IEEE Access*, vol. 9, pp. 163 431–163 440, 2021.

[7] L. Xu *et al.*, "Comparative Analysis of Numerical Methods for Lithium-Ion Battery Electrochemical Modeling," *J. Electrochem. Soc.*, vol. 170, no. 12, p. 120525, Dec. 2023.

[8] S. Fasolato and D. M. Raimondo, "Observability analysis of a Li-ion cell equivalent circuit model based on interval arithmetic," in *2022 IEEE Vehicle Power and Propulsion Conference (VPPC)*. Merced, CA, USA: IEEE, Nov. 2022, pp. 1–7.

[9] R. LeVeque, *Finite Difference Methods for Ordinary and Partial Differential Equations: Steady-State and Time-Dependent Problems*, ser. Other Titles in Applied Mathematics. Society for Industrial and Applied Mathematics, 2007.

[10] G. Plett and M. Trimboli, *Battery Management Systems, Volume III: Physics-Based Methods*, ser. Artech House power engineering series. Artech House, 2024, no. v. 3.

[11] R. Hermann and A. Krener, "Nonlinear controllability and observability," *IEEE Trans. Automat. Contr.*, vol. 22, no. 5, pp. 728–740, Oct. 1977.

[12] H. Nijmeijer and A. van der Schaft, *Nonlinear Dynamical Control Systems*. Springer, 1990.

[13] W. R. Inc., "Mathematica, Version 14.1," Champaign, IL, 2024. [Online]. Available: https://www.wolfram.com/mathematica

[14] L. Trefethen and D. Bau, *Numerical Linear Algebra*, ser. Other Titles in Applied Mathematics. Society for Industrial and Applied Mathematics (SIAM, 3600 Market Street, Floor 6, Philadelphia, PA 19104), 1997.

[15] Y. Gao, T. Nguyen, and S. Onori, "Model-Based State-of-Charge Estimation of 28 V $LiFePO_4$ Aircraft Battery," *SAE Int. J. Elec. Veh.*, vol. 14, no. 1, pp. 14–14–01–0003, Aug. 2024.

[16] J. Wilson and S. Guhe, "Observability matrix condition number in design of measurement strategies," in *Computer Aided Chemical Engineering*. Elsevier, 2005, vol. 20, pp. 397–402.

[17] G. Richardson *et al.*, "Generalised single particle models for high-rate operation of graded lithium-ion electrodes: Systematic derivation and validation," *Electrochim. Acta*, vol. 339, p. 135862, Apr. 2020.

[18] C.-H. Chen *et al.*, "Development of Experimental Techniques for Parameterization of Multi-scale Lithium-ion Battery Models," *J. Electrochem. Soc.*, vol. 167, no. 8, p. 080534, Jan. 2020.

[19] Y. Zeng *et al.*, "Efficient Conservative Numerical Schemes for 1D Nonlinear Spherical Diffusion Equations with Applications in Battery Modeling," *J. Electrochem. Soc.*, vol. 160, no. 9, pp. A1565–A1571, 2013.

[20] G. Pozzato, A. Allam, and S. Onori, "Lithium-ion battery aging dataset based on electric vehicle real-driving profiles," *Data in Brief*, vol. 41, p. 107995, Apr. 2022.

[21] J. N. E. Lucero, L. Xu, and S. Onori, "Observability analysis of a Li-ion cell equivalent circuit model based on interval arithmetic," in *2024 IFAC Modeling Estimation and Control Conference (MECC)*. IFAC, october 2024, pp. 1–6.

[22] A. M. Bizeray *et al.*, "Identifiability and Parameter Estimation of the Single Particle Lithium-Ion Battery Model," *IEEE Trans. Contr. Syst. Technol.*, vol. 27, no. 5, pp. 1862–1877, Sep. 2019.

[23] J. N. E. Lucero, M. Uppaluri, and S. Onori, "Structural Identifiability of Electrochemical Lithium-Ion Battery Models," 2025, In preparation.

[24] G. Pozzato *et al.*, "Core-Shell Enhanced Single Particle Model for lithium iron phosphate Batteries: Model Formulation and Analysis of Numerical Solutions," *J. Electrochem. Soc.*, vol. 169, no. 6, p. 063510, Jun. 2022.

[25] M. Doyle, T. F. Fuller, and J. Newman, "Modeling of Galvanostatic Charge and Discharge of the Lithium/Polymer/Insertion Cell," *J. Electrochem. Soc.*, vol. 140, no. 6, pp. 1526–1533, Jun. 1993.